

Structural Optimization in Tensor LEED Using a Parameter Tree and R -Factor Gradients

Alexander M. Imre,¹ Paul Haidegger,¹ Florian Kraushofer,¹ Ralf Wanzenböck,²
Tobias Hable,¹ Sarah Tobisch,¹ Marie Kienzer,¹ Florian Buchner,² Jesús Carrete,³
Georg K. H. Madsen,² Michael Schmid,¹ Ulrike Diebold,¹ and Michele Riva^{1,*}

¹*Institute of Applied Physics, TU Wien, Vienna, Austria*

²*Institute of Materials Chemistry, TU Wien, Vienna, Austria*

³*Instituto de Nanociencia y Materiales de Aragón (INMA), CSIC-Universidad de Zaragoza, Zaragoza, Spain*
(Dated: December 11, 2025)

Quantitative low-energy electron diffraction [LEED $I(V)$] is a powerful method for surface-structure determination, based on a direct comparison of experimentally observed $I(V)$ data with computations for a structure model. As the diffraction intensities I are highly sensitive to subtle structural changes, local structure optimization is essential for assessing the validity of a structure model and finding the best-fit structure. The calculation of diffraction intensities is well established, but the large number of evaluations required for reliable structural optimization renders it computationally demanding. The computational effort is mitigated by the tensor-LEED approximation, which accelerates optimization by applying a perturbative treatment of small deviations from a reference structure. Nevertheless, optimization of complex structures is a tedious process.

Here, the problem of surface-structure optimization is reformulated using a tree-based data structure, which helps to avoid redundant function evaluations. In the new tensor-LEED implementation presented in this work, intensities are computed on the fly, eliminating limitations of previous algorithms that are limited to precomputed values at a grid of search parameters. It also enables the use of state-of-the-art optimization algorithms. Implemented in PYTHON with the JAX library, the method provides access to gradients of the R factor and supports execution on graphics processing units (GPUs). Based on these developments, the computing time can be reduced by more than an order of magnitude.

I. INTRODUCTION

Low-energy electron diffraction (LEED) is a widely utilized technique in modern surface science due to its ability to quickly provide information on the structure of single-crystal surfaces. A sharp diffraction pattern confirms the long-range order and reveals the periodicity and symmetry of the surface structure. Beyond qualitative analysis, quantitative examination of diffraction intensities as a function of the incident electron energy, producing so-called $I(V)$ curves, offers deep insights into the atomic-scale arrangement of the surface, requiring only small investment in additional instrumentation. LEED $I(V)$ combines surface sensitivity with high precision, making the method a valuable tool for the analysis of surface structures [1–8].

Similarly to x-ray diffraction, LEED diffraction intensities encode information about atomic positions and vibration amplitudes on the picometer scale. However, unlike x-rays, the electrons used in LEED $I(V)$ —with typical energies ranging from fifty to a few hundred electronvolts—have an inelastic mean free path of only a few atomic layers [9]. As a result, the elastically scattered electrons that contribute to the diffraction intensities interact only with the uppermost atomic layers. In addition, elastic-scattering cross sections are large, leading to

strong contributions of multiply scattered electrons to the diffraction signal and enhancing the sensitivity to small structural changes. This unique combination of surface specificity and high sensitivity to interatomic distances makes LEED $I(V)$ the most successful method to verify or exclude structure models of surfaces [5–8].

Unfortunately, like most diffraction techniques, LEED $I(V)$ suffers from the well-known phase problem, where only the intensities of the diffracted beams are accessible in the experiment. The loss of the phase information and the contributions of multiple scattering make it impossible to directly derive the atomic positions from the measured intensities (with the exception of selected cases where holographic LEED or other “direct” methods can aid structure determination [10–13]). Instead, a LEED- $I(V)$ study requires an initial structure model (a result of a search using computational methods or a human “guess”), calculating the diffraction intensities for this model and refining the model by minimizing the disagreement between calculated and experimental $I(V)$ data. Thereby, qualitatively different structures can be evaluated and the parameters (such as the exact atomic positions) of a structure model can be determined.

Despite considerable progress in terms of usability and performance of LEED $I(V)$ calculations [7, 14], the search for a best-fit structure is computationally expensive and often requires human intervention. With the currently most widely used programs, search is limited to a discrete grid and geometrical optimization is restricted to one direction at a time. This makes LEED $I(V)$ poorly

* Corresponding author: riva@iap.tuwien.ac.at

sued for automated structure search, for instance, to assess the validity of structure models generated by machine-learning (ML) algorithms based on density-functional theory (DFT). The current work presents a new implementation for structural search by LEED $I(V)$, which does not suffer from the limitations discussed above. Describing search parameters as a tree structure paves the way for the use of state-of-the-art search algorithms and computational optimization. Taking advantage of graphics processing units (GPUs) and automatic differentiation to calculate R -factor gradients, the new implementation greatly reduces the computing time.

A. Basics of LEED- $I(V)$ Calculations

Theoretical modeling of $I(V)$ curves is a non-trivial task. As mentioned in Section I, the calculation must account for multiple scattering, also known as a “full-dynamic” calculation. Techniques for solving this problem were first described by Pendry, Tong, van Hove, and collaborators in the 1970s, and many of their methods form the basis of LEED- $I(V)$ calculations today [1–4, 15]. Various codes have been developed over the years that can perform these calculations, each with their own strengths and target audiences [16–23].

Today’s LEED codes are based on the muffin-tin approximation, with a constant potential V_0 (also referred to as inner potential) for the interstitial region and a spherical potential well for each atom [1, 7]. Based on this potential, scattering phase shifts can be calculated that describe a single scattering event of an incident electron wave with the scattering atoms [24–27].

Under that approximation, atoms are reduced to point scatterers that impart phase shifts onto the incoming electron wave. The atoms are then grouped into crystal layers, and intra- and inter-layer scattering is calculated. The scattering in between such layers is treated using plane waves, whereas the scattering within a layer uses a spherical-wave expansion. This expansion is truncated at a maximum angular momentum quantum number ℓ_{\max} . The choice of ℓ_{\max} is a trade-off between accuracy and computational cost, since the size of most intermediate tensors in the calculation scales with powers of ℓ_{\max} up to $(\ell_{\max}+1)^4$, and the number of floating-point operations scales with up to $(\ell_{\max}+1)^6$.

Diffraction from the bulk crystal is modeled by infinitely repeating bulk-like layers at the bottom of the structure. The final diffraction intensities are obtained by considering transmission, reflection, and attenuation for each crystal layer, and summing the possible diffraction paths [2, 15].

B. The Optimization Problem

Because LEED $I(V)$ is extremely sensitive to structural details—down to picometer-scale changes in atomic

positions—a single calculation of diffraction intensities is insufficient to assess the validity of a structure model. Even for structures relaxed by DFT, the deviations between the calculated and actual coordinates may be large enough to yield a poor R factor when compared to experiment; this may depend on the choice of the DFT functional [28]. Consequently, a valid structure model may be misjudged as incorrect. Thus, a local optimization against experimental data is required, even when only a qualitative yes/no decision is sought.

For structure optimization, the disagreement between calculated and experimental $I(V)$ curves is quantified by a single number, the R factor, which should be minimized. The most commonly used R factors are those of Zannazi and Jona [29] and Pendry [30], with the latter being the preferred choice in most cases [16, 31, 32]. Recently, the authors of this article proposed a new “smooth” R factor [33], which addresses several shortcomings in its formulation.

The optimization problem can be formulated in terms of the model parameters: the atomic coordinates \mathbf{r}_i , the mean vibration amplitudes $v_i = \sqrt{\langle u_i^2 \rangle_T}$, and, in case of substitutional alloys, compounds, or structures with (disordered) vacancies, the statistical occupancy values (concentrations) c_i [34]. Here, the index i runs over all scattering centers in the unit cell, that is, all geometric sites and all chemical species that may occupy them. In addition, diffraction intensities also depend on nonstructural parameters (collectively denoted by μ in the following), such as the offset V_{00} of the real part of the inner potential [35]. For any vector $\xi = \{\mathbf{r}_i, v_i, c_i, \mu\}$ of these input parameters (including all scattering centers i), the diffraction intensities $I_{\mathbf{g}}^{\text{calc}}(\xi)$ can be calculated for all diffraction orders \mathbf{g} and all electron energies. These calculated intensities are compared to the experimental data $I_{\mathbf{g}}^{\text{exp}}$ through the associated R factor, $R(I_{\mathbf{g}}^{\text{calc}}(\xi); I_{\mathbf{g}}^{\text{exp}})$.

This leads to a high-dimensional optimization problem with the R factor as the objective function:

$$\min_{\xi} R(I_{\mathbf{g}}^{\text{calc}}(\xi); I_{\mathbf{g}}^{\text{exp}}). \quad (1)$$

Any approach to tackle such a high-dimensional optimization problem inevitably requires a huge number of evaluations of the objective function, each involving the calculation of a full set of diffraction intensities.

While full-dynamic calculations give access to the $I(V)$ curves $I_{\mathbf{g}}^{\text{calc}}(\xi)$ for arbitrary ξ , this calculation is computationally expensive [36]. A single reference calculation on a state-of-the-art workstation or supercomputer node requires on the order of minutes for anything but the smallest unit cells [14], and many hours for large structures [37, 38]. Although this cost is acceptable for single-shot calculations, it becomes prohibitive in a structure-optimization loop with a large parameter space.

C. The Tensor-LEED Approximation

To overcome the computational bottleneck of full-dynamic calculations, the so-called tensor-LEED approximation was introduced by Rous *et al.* [39–41]. It treats small changes to an initial “reference” structure via a perturbative approach. Compared to an optimization using only full-dynamic calculations, this substantially reduces the computational cost and therefore accelerates structure optimization by several orders of magnitude. Perturbations to the reference structure may be geometric displacements of atoms, changes of vibration amplitudes, or even chemical substitutions [42–44]. If the reference structure is denoted as

$$\xi^{\text{ref}} = \{\mathbf{r}_i^{\text{ref}}, v_i^{\text{ref}}, c_i^{\text{ref}}, \mu^{\text{ref}}\} \quad (2)$$

and the perturbation as

$$\delta\xi = \{\delta\mathbf{r}_i, \delta v_i, \delta c_i, \delta\mu\}; \quad (3)$$

then the perturbed structure is given by

$$\xi = \xi^{\text{ref}} + \delta\xi. \quad (4)$$

The intensities of the diffracted beams are then given by

$$I_{\mathbf{g}} = |A_{\mathbf{g}}^{\text{ref}} + \delta A_{\mathbf{g}}(\delta\xi)|^2, \quad (5)$$

where the amplitude changes $\delta A_{\mathbf{g}}$ (sometimes also called “delta amplitudes”) are a function of $\delta\xi$. In tensor LEED, the amplitude changes for any beam \mathbf{g} are approximated by a linear combination of the amplitude changes for each scattering center i in the unit cell [45],

$$\delta A_{\mathbf{g}} = \sum_i \delta A_{i,\mathbf{g}}. \quad (6)$$

Nonstructural parameters μ can affect both the individual $\delta A_{\mathbf{g}}$ and the overall R -factor calculation.

Tensor LEED is a first-order perturbation theory with respect to the influence of the scattering matrices t_i on the amplitudes $\delta A_{\mathbf{g}}$. Nevertheless, the amplitude changes $\delta A_{i,\mathbf{g}}$ are highly nonlinear functions of the atomic displacements. This nonlinearity is illustrated in Section S1 of the Supporting Information [46]. Consequently, a simple linearization of the diffraction amplitudes (or intensities) is not possible, and the optimization problem posed in Section IB remains nontrivial.

D. ViPERLEED

The current work is based on ViPERLEED, an integrated package for LEED- $I(V)$ experiments and simulations [14, 47–49]. Its VIPERLEED.CALC PYTHON package provides calculations of diffraction intensities, structure optimization, and comparison of calculated and experimental $I(V)$ curves. Internally, VIPERLEED.CALC uses the Erlangen tensor-LEED package (TENSERLEED) [21] for most calculations [50].

E. Optimization in TENSERLEED and viperleed.calc

In TENSERLEED, for computational efficiency, the parameter space is sampled on a user-defined grid [21, 51]. For every atom, the user can specify a set of geometric displacements, vibration amplitudes, and occupancies to be considered during the optimization. Based on the user input, the code first calculates the amplitude changes $\delta A_{i,\mathbf{g}}$ for all scatterers i and requested grid points. During the minimization, for each configuration sampled, $\delta A_{\mathbf{g}}$ is calculated as a linear combination of the $\delta A_{i,\mathbf{g}}$ [see Eq. (6)] and the R factor is calculated by comparing the calculated diffraction intensities to the experimental data. The parameter combination that achieves the minimum R factor is referred to as the best-fit structure.

While the method used in TENSERLEED is effective, it also has several shortcomings that lead to inefficiencies. The calculation of $\delta A_{i,\mathbf{g}}$ is strictly separated from the optimization step, and the optimization itself is grid-based. The step width—and thus the achievable precision of the optimized structure—must be fixed before the optimization loop begins. In addition, atoms can only be displaced along a one-dimensional trajectory, which restricts the search space and leaves many configurations inaccessible. Thus, an iterative approach is required to optimize atomic positions in three-dimensional (3D) space.

VIPERLEED.CALC includes some provisions to work around these issues as described in Ref. 14, although it cannot completely circumvent them. The structure optimization remains the bottleneck of the calculation, especially for large and complex surface structures, and often takes more than 90% of the total calculation time.

Additionally, the structure optimization is often the most problematic step in a LEED- $I(V)$ study from a user perspective. An inexperienced user may select parameters (such as the step sizes) with which the optimization algorithm can become trapped at a local minimum. The grid-based nature of the optimization and the limitation to one-dimensional atomic displacements make it difficult to set up the optimization efficiently.

II. TENSOR LEED USING PYTHON, JAX, AND AUTOMATIC DIFFERENTIATION

Despite the sophistication of the R -factor-minimization algorithm [51] used in TENSERLEED, its improvements in ViPERLEED, and further efforts to develop optimization methods tailored to LEED- $I(V)$ [16, 52–59], existing implementations often remain tightly coupled to specific systems or surface geometries. While effective in context, this limits their generality. Here, a more abstract formulation of LEED- $I(V)$ structure optimization is introduced to improve transferability across systems.

A. High-Dimensional Optimization and Automatic Differentiation

As mentioned in Section IB, structure optimization in LEED $I(V)$ is a high-dimensional numerical optimization problem. As such, it can (and should) be tackled by modern numerical optimization algorithms that have been developed over the past decades. Advances in fields such as machine learning have led to the development of highly efficient and robust optimization algorithms that can be applied to a wide range of problems [60–62].

Today, optimization can also make use of automatic-differentiation libraries that provide an efficient calculation of gradients for a wide range of functions. While this development has been primarily driven by the machine-learning community and the demand for efficient back-propagation algorithms, the applications of automatic differentiation are not limited to the field [63–65]. Several machine-learning frameworks exist that support automatic differentiation and highly parallelized execution on graphics-processing units (GPUs) such as TENSORFLOW [66], PYTORCH [67], and JAX [68]. The latter is used in the tensor-LEED implementation of this work.

B. Application to Tensor LEED

A generalized framework for structure optimization within LEED $I(V)$ and VIPERLEED.CALC is presented, based on a reworked tensor-LEED implementation with four key improvements:

1. Automatic interpretation and dimensionality reduction of the parameter space using symmetry and user-defined constraints (Section III and Sections S6–S9 of the Supporting Information [46]). This approach enables all parameter changes (i.e., perturbations) to be represented by a single, normalized, real-valued vector.
2. Exploitation of symmetry and composed transformations to minimize redundant evaluations of functions (e.g., spherical harmonics) at each scattering center. This substantially reduces computational cost and is especially valuable for complex systems.
3. Implementation in PYTHON with the JAX library [68], which supports GPU execution and provides gradients of the R -factor hypersurface by automatic differentiation (Sections IV and V). This enables the use of gradient-based optimizers.
4. Integration of these improvements to enable the application of established algorithms to the optimization problem. The task is separated into an exploratory (i.e., global) search for the best-fit structure followed by a local refinement (Sections V and VI).

This new implementation, named VIPERLEED-JAX, takes a different approach than TENSORLEED: The calculation of the amplitude changes $\delta A_{\mathbf{g}}$ is incorporated into the structure-optimization step and done on the fly as required. This allows calculating the R factor at any point in the parameter space, and removes the need for a grid-based method. As discussed in Sections V and VI, while this is computationally more expensive per configuration, it improves the performance of the search, leading to an altogether faster convergence.

III. ENCODING THE PARAMETER SPACE

The parameter space for a tensor-LEED calculation is usually high-dimensional. While the full set of mathematically possible perturbations is given by the combination of 3D geometric displacements $\delta \mathbf{r}_i$, changes of vibration amplitudes δv_i , and fractional occupancy values δc_i for all scattering centers, plus nonstructural parameters $\delta \mu$, the effective parameter space is much smaller. Symmetry (which is detected automatically in VIPERLEED.CALC, but can be overridden by the user) restricts the set of valid perturbations. Furthermore, users commonly impose additional constraints on the perturbations, such as linked vibration amplitudes or concerted atomic displacements, to conform with physical intuition or avoid overfitting. Even if these constraints are not directly required by symmetry, they may be necessary to ensure that the optimization problem is well posed.

A. Linear Transformations of Parameters

A constraint on the parameters ξ reduces the number of degrees of freedom of the optimization problem. If one considers, for example, a symmetry constraint that links two or more symmetry-equivalent atoms, the number of free geometric parameters of this group of atoms is reduced to a total of (at most) three. The displacements $\delta \mathbf{r}_{a,b}$ of two symmetry-equivalent atoms a and b are linked by a linear symmetry operation \mathbf{M} as

$$\delta \mathbf{r}_b = \mathbf{M} \delta \mathbf{r}_a. \quad (7)$$

Equivalently, any such symmetry-linked displacement $\delta \mathbf{r}_i$ may be described by a single parameter vector \mathbf{p}_k , such that

$$\delta \mathbf{r}_i = X_{i,k}^{\text{sym}} \mathbf{p}_k, \quad (8)$$

where the transformations $X_{i,k}^{\text{sym}}$ encode the symmetry information of the system.

A user may further choose to constrain the system, for instance, by linking out-of-plane displacements of non-symmetry-equivalent atoms in a crystal layer. In this case, the displacements of the atoms can be described by a second linear transformation $X_{j,k}^{\text{link}}$ acting on an even

smaller set of parameters \mathbf{t}_k as given by

$$\delta \mathbf{r}_i = X_{i,j}^{\text{sym}} X_{j,k}^{\text{link}} \mathbf{t}_k. \quad (9)$$

In both cases, the constraints reduce the number of degrees of freedom of the system, and allow determining the full set of displacements $\delta \mathbf{r}_i$ ($3n$ values for n linked atoms) through a linear transformation applied to \mathbf{t}_k (a maximum of three values).

It should be noted that there are also nonlinear constraints, which cannot be expressed as linear transformations. Section S10 of the Supporting Information [46] shows that the occupancy parameters (concentrations) are such a case and how this can be handled in the current framework.

B. Irreducible Parameter Space

The full set of parameters, $\xi = \{\mathbf{r}_i, v_i, c_i, \mu\}$ [69], belongs to a vector space Ξ . Constraints reduce the degrees of freedom of the system and can be expressed as (linear) transformations acting on the parameters. This allows the full parameter set ξ to be uniquely determined by a reduced set ξ^{red} from a subspace Ξ^{red} , with

$$\dim(\Xi^{\text{red}}) \leq \dim(\Xi). \quad (10)$$

The mapping f^{red} ,

$$f^{\text{red}} : \Xi^{\text{red}} \rightarrow \Xi, \quad (11)$$

is injective, meaning that no two distinct reduced parameter sets ξ^{red} map to the same full set ξ .

By applying all constraints, a final set of “irreducible” parameters, $\tilde{\xi}$, is obtained. These parameters belong to the irreducible subspace $\tilde{\Xi}$, where

$$\tilde{\xi} \in \tilde{\Xi}, \quad \dim(\tilde{\Xi}) \leq \dim(\Xi). \quad (12)$$

Consequently, the vector ξ of full parameters, can be uniquely determined from the irreducible vector $\tilde{\xi}$ through an injective mapping

$$f : \tilde{\Xi} \rightarrow \Xi, \quad \tilde{\xi} \mapsto \xi = f(\tilde{\xi}). \quad (13)$$

The mapping f encodes all constraints on the parameters ξ , and converts any $\tilde{\xi}$ to a set of input values for the tensor-LEED calculation [69]. In other words, $f(\tilde{\Xi})$ spans the constrained parameter space within Ξ , covering all valid configurations of ξ . The optimization algorithm works in the irreducible parameter space. The mapping f translates each point ξ probed by the optimization algorithm to an input for the tensor-LEED calculation.

C. Tree-like Representation of the Parameter Space

Borrowing concepts from graph theory, the application of constraints can be represented using a tree-like data

structure, similar to computational graphs in automatic differentiation and machine learning [64]. Value propagation in this “parameter tree” helps to reduce the number of function evaluations needed to calculate the R factor and its gradient.

Nodes in the tree (Fig. 1) represent scalar- or vector-valued parameters, and edges correspond to linear or affine transformations between them. The leaf nodes contain the full set of parameters ξ of the tensor-LEED calculation [69], while the root nodes form the irreducible set of free parameters $\tilde{\xi}$. Fig. 1 highlights the hierarchical structure of the parameter space and the mapping between full and irreducible parameter sets via multiple layers of constraints.

Each non-leaf, non-root node has a single parent and one or more children. The values of each child node are obtained by applying the transformation X_e associated with the edge e to the value of the parent node. Constraints are naturally applied in a bottom-up manner: starting from the leaves and narrowing the parameter space toward the roots. Although the order of constraints does not affect the uniqueness of the mapping between full and irreducible parameters, applying symmetry constraints first is advantageous, as these are the most fundamental ones and make the construction of the tree more efficient.

All parameters have user-specified bounds (e.g., a range for displacements). These bounds may reflect physical limitations, since the tensor-LEED approximation is only valid for small perturbations, and vibration amplitudes must be positive. For optimization, all parameter values are normalized such that the components of the irreducible parameters $\tilde{\xi}_j$ lie in the $[0, 1]$ interval, as indicated in Fig. 1. Details of the normalization are given in Section S9 of the Supporting Information [46].

D. Properties of the Parameter Tree

Sections III E–III G describe how the tree-like representation of the parameter space can be used and leveraged. To facilitate this discussion, some properties of the tree and the transformations applied to the parameters are introduced here.

1. Linearity

Each edge in the tree, connecting a parent node n to a child node n' , is assumed to represent an affine transformation $X_{n',n}$ of the form

$$X_{n',n}(p) = M_{n',n}p + b_{n',n}, \quad (14)$$

where $M_{n',n}$ is the matrix of a linear transformation acting on the (scalar or vectorial) parameter p , and $b_{n',n}$ a translation. Except for normalization to the $[0, 1]$ range of the irreducible parameters $\tilde{\xi}$, the transformations are

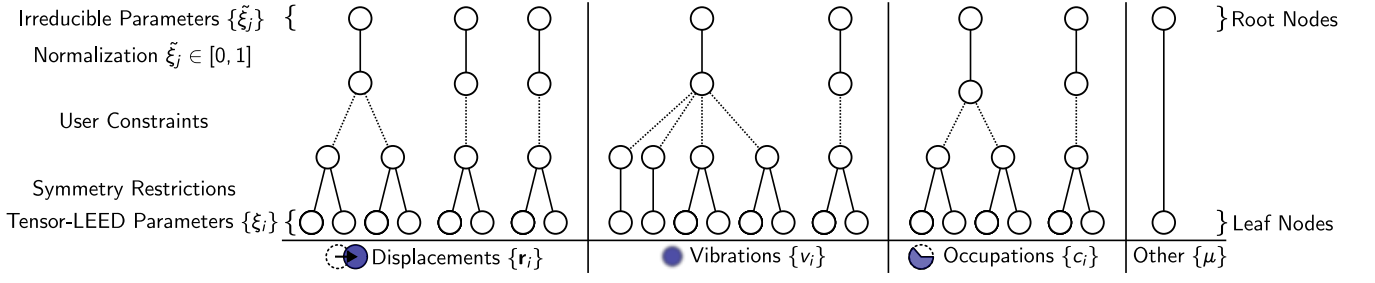


FIG. 1. Schematic representation of the parameter tree. The input parameters of the tensor-LEED calculation are $\xi = \{\xi_i\} = \{\mathbf{r}_i, v_i, c_i, \mu\}$ [69]. They are linked to the vector of irreducible parameters $\tilde{\xi} = \{\tilde{\xi}_j\}$ via system and user constraints. Dashed lines represent links due to user constraints, which depend on user input and may be changed. Solid lines represent links which are automatically created and do not depend on user inputs (symmetry restrictions and normalizations).

linear mappings, without a translation (i.e., $b_{n',n} = 0$ in Eq. (14); see Section S8 of the Supporting Information [46]). Affine transformations are efficiently implemented using matrix–vector multiplication and addition. Since the tree is constructed only once per optimization run, its computational overhead is negligible.

2. Composability and the Mapping Function

The transformation X_{n_0, n_k} between any two nodes n_0 and n_k is obtained by composing the transformations along the path connecting them:

$$X_{n_0, n_k} = X_{n_0, n_1} \circ X_{n_1, n_2} \circ \cdots \circ X_{n_{k-1}, n_k}, \quad (15)$$

where n_1, n_2, \dots, n_{k-1} are the intermediate nodes along the path.

Thus, the mapping f [Eq. (13)] from irreducible parameters $\tilde{\xi}$ to the full parameters set ξ is obtained by composing the transformations along the path connecting the corresponding nodes:

$$\xi_i = f(\tilde{\xi}_j) = X_{i,j}(\tilde{\xi}_j). \quad (16)$$

3. Invertibility

For some calculations (dependent quantities, see Section III E, propagation of bounds, see Section S9 of the Supporting Information [46]), it is necessary to determine the transformation from a child node n' to its parent n , $X_{n, n'}$, which is the inverse of $X_{n', n}$. Affine transformations are not always invertible; for example, a symmetry-violating displacement cannot be expressed in terms of irreducible parameters. However, as mentioned in Section III B, all transformations considered here are injective. A non-invertible case cannot occur because the values at the child node n' always lie in the image of $X_{n', n}$. For the injective linear transformations considered here (see also Section S8 of the Supporting Information [46]), the inverse exists and is given by the Moore–Penrose pseudoinverse [70].

E. Tree Traversal and Dependent Quantities

Since the transformations corresponding to the edges of the parameter tree are invertible, the transformation between two nodes with the same root can be computed. For instance, within a group of linked atoms the displacement $\delta \mathbf{r}_i$ of atom i can be expressed in terms of the displacement $\delta \mathbf{r}_{i'}$ of a reference atom i' as

$$\delta \mathbf{r}_i = X_{i, i'} \delta \mathbf{r}_{i'}. \quad (17)$$

Here, $X_{i, i'} = X_{i, a} \circ X_{a, i'}$ denotes the composed transformation between nodes i and i' , obtained by traversing the tree upward from the reference atom i' to a common ancestor node a , and then downward to atom i .

Although seemingly trivial, this relation is central to a highly efficient implementation of tensor LEED, since the change in the diffraction amplitudes is obtained as a superposition of atomic contributions $\delta A_{i, \mathbf{g}}$ [39, 40], as given in Eq. (6). The evaluation of $\delta A_{i, \mathbf{g}}$ for each vector of parameter variations $\delta \xi_i$ dominates the computational cost, as it requires many evaluations of computationally expensive functions (spherical Bessel functions, spherical harmonics) for each scattering center. Since displacements of linked atoms can be obtained from those of a reference atom via composed transformations, only a reduced set of atomic contributions $\delta A_{i, \mathbf{g}}$ needs explicit computation. This avoids redundant evaluations and yields substantial efficiency gains. The strategy is referred to here as “dependent quantities” and is detailed in Section S5 of the Supporting Information [46].

F. Atoms as Leaf Nodes

Sections S7 and S8 of the Supporting Information [46] discuss the practical construction of the parameter tree for a tensor-LEED calculation. The tree is built from the leaves upward to the root, with symmetry relations and user-defined constraints enforced along the way. This construction is not only suited for structural optimization, but also provides a systematic means of verifying the consistency of user-imposed constraints.

As introduced in Section IB, the input parameters for a tensor-LEED calculation are given by $\xi = \{\mathbf{r}_i, v_i, c_i, \mu\}$ [69], where i indexes all scattering centers, encompassing the geometric sites and, in the case of mixed occupancy, all chemical species that may occupy them. A natural choice is therefore to assign leaf nodes to each scattering center and parameter type (geometric, vibrational, occupancy). To ensure consistent handling, the nonstructural parameters μ are included as additional leaf nodes, as illustrated in Fig. 1.

G. Bounds, Implicit Constraints, and Normalization

As mentioned in Section III B, the optimization problem of Eq. (1) is subject to bounds on the parameters ξ_i ,

$$\xi_i^{\text{lower}} \leq \xi_i \leq \xi_i^{\text{upper}}. \quad (18)$$

Parameters can also be completely fixed (e.g., restricting an atom to displacements normal to the surface plane even in the absence of symmetry constraints that fix the x and y coordinates). Such fixed parameters act as implicit constraints, reducing both the number of degrees of freedom and the dimensionality of the vector $\tilde{\xi}$ of irreducible parameters.

Both bounds and implicit constraints can be incorporated directly into the mapping function f of Eq. (13). By construction, f maps the irreducible parameters $\tilde{\xi}_j \in [0, 1]$ onto the full parameters $\xi_i \in [\xi_i^{\text{lower}}, \xi_i^{\text{upper}}]$. This formulation ensures that any optimization algorithm operates on normalized parameter vectors $\tilde{\xi}$ with equally weighted components, which can improve convergence. Implementation details for this normalization can be found in Section S9 of the Supporting Information [46] [71].

IV. IMPLEMENTATION IN VIPERLEED-JAX

The new developments for tensor LEED described above are realized in VIPERLEED-JAX [72]. Written entirely in PYTHON, it is distributed as open-source software under the GNU General Public License version 3 (or later) [73]. This implementation can be chosen to replace the TENSERLEED-based structure optimization of VIPERLEED.CALC [14], which is released under the same license.

A. Parameter Tree Implementation

The code is designed to be modular and easily extensible, enabling adaptation to specific applications. In particular, the tree-like parameter representation is implemented separately from the optimization routines and

includes several layers of abstraction. It depends only on the NUMPY [74], SCIPY [75], and ANYTREE [76] packages. This separation facilitates extension to problems beyond LEED $I(V)$ or the incorporation of additional types of constraints or nonstructural parameters.

B. Tensor-LEED Implementation in JAX

The new tensor-LEED code in VIPERLEED-JAX makes use of the output of the full-dynamic calculation (the “reference calculation”) of VIPERLEED.CALC (which internally uses the TENSERLEED code) and keeps compatibility with the data formats of VIPERLEED.CALC. The calculation of the $I(V)$ curves by tensor LEED, the calculation of the R factor and the search have been entirely re-implemented in PYTHON and JAX [68] to enable end-to-end differentiability and just-in-time compilation for GPU-accelerated execution. Most required mathematical functions are available in JAX’s standard libraries, with additional functionality supplied by the NEURALIL package [77] for spherical Bessel functions and the INTERPAX package [78] for spline interpolations. The implementation is designed as a plugin for VIPERLEED.CALC, serving as an optional substitute for the TENSERLEED-based structure search.

To support automatic differentiation and efficient tensor contractions, several computational strategies and best practices are employed. Selected techniques are discussed in Section S4 of the Supporting Information [46], including the use of precalculated Gaunt coefficients, evaluated with SYMPY [79] and stored according to a scheme inspired by Rasch and Yu [80].

V. SEARCH ALGORITHMS

The R -factor hypersurface, $R(\tilde{\xi})$, depends on the surface structure and the chosen R factor, and is a highly nonlinear function of the parameters $\tilde{\xi}$ with numerous local minima [3, 51]. Finding the global minimum becomes increasingly difficult as the number of parameters increases.

No single algorithm is universally optimal, and the choice of method depends on the specific problem [81]. The approach presented in Section III reduces the structure optimization in LEED $I(V)$ to a standard bounded numerical optimization problem. Thus, the R factor can be treated as a black-box objective function that takes the normalized irreducible parameters $\tilde{\xi}$ as input and returns a single scalar value, optionally with a gradient. This makes it easy to try different algorithms among the large number of optimization methods developed for numerical optimization. In the present work, several readily accessible methods were compared. The focus, however, was on demonstrating the optimization framework rather than performing exhaustive benchmarking or run-time tuning.

A two-stage optimization strategy [82] was found to be the most reliable to locate the global minimum of the R -factor hypersurface. In this approach, the optimization is split into an exploratory stage, which aims to identify the region containing the global minimum within the parameter bounds, and a local stage, which refines the structure in this region. The exploratory and local stages may employ different optimization algorithms tailored to their respective tasks.

A. Exploratory Search Using CMA-ES

The first, exploratory stage of the search has the task of finding the basin of the global minimum. Simple parameter-wise optimization was found to be insufficient, as it is highly susceptible to trapping into local minima. Basin hopping [83], as implemented in SCIPY [75], was also found to be inefficient, due to the computational cost of evaluating the gradient ∇R across large regions of the parameter space.

The covariance-matrix-adaptation evolution strategy (CMA-ES) is a robust optimization algorithm, particularly suitable for high-dimensional, nonlinear problems. It provides a balance between exploration and exploitation, is robust against local minima, and does not require evaluation of gradients [84, 85]. Similar to the search algorithm in TENSORLEED [51], it is based on generations of point clouds drawn from multivariate normal (Gaussian) distributions. Compared to the algorithm in TENSORLEED, one of the advantages of CMA-ES is a sophisticated method for adapting the covariance matrix of the distribution to the R -factor hypersurface.

The CMA-ES implementation from the CLINAMEN2 package [86] was employed due to its efficiency and compatibility with the PYTHON- and JAX-based framework. Because the standard CMA-ES implementation does not support parameter bounds, adaptations were applied to operate within a bounded parameter space. Details of this adaptation are provided in Section S11 of the Supporting Information [46].

B. Switching from Exploratory to Local Optimization

The two-stage approach requires a convergence criterion for switching from the exploratory stage to local refinement. While it is impossible to identify the global minimum with absolute certainty, it is easier to determine whether the exploratory optimization has converged on a single attraction basin. Once this happens, the transition from the exploratory stage to the local one should be made.

To identify this basin is not trivial; several approaches are possible. In this work, a threshold ($\approx 5 \times 10^{-3}$) was applied to the standard deviation of R factors within a single CMA-ES generation. Once this threshold is

reached, the optimization proceeds to the local stage. This criterion is based on the assumption that when CMA-ES generates configurations with similar R -factor values, the algorithm has likely identified the desired region. Alternatively, a criterion based on R -factor changes between generations could be conceived.

Information obtained during the exploratory stage can be used to improve the local optimization. For example, the covariance matrix estimated in CMA-ES is proportional to the inverse of the Hessian of the R -factor hypersurface [87] and can serve to precondition the local refinement, as discussed Section S12 of the Supporting Information [46].

C. R -Factor Gradients for Local Refinement

In optimization, the availability of gradients is known to improve optimization efficiency by indicating the direction of steepest descent. Previous structure-optimization implementations in tensor LEED have not used analytical gradients of the R -factor hypersurface. This limitation has been noted in the literature [3, 18, 56], and existing methods either rely on gradient-free algorithms or on finite-difference approximations [55].

With the automatic-differentiation capabilities of JAX, the gradient ∇R of the R -factor hypersurface with respect to the irreducible parameters ξ can be calculated. Most functions in the tensor-LEED calculation are differentiable, but some cases require special treatment, such as the transformation between Cartesian and spherical coordinates [88]. Details of these cases are provided in Section S4 of the Supporting Information [46].

The calculation of the R -factor gradient is computationally more expensive than a simple evaluation of the R factor, since gradients require the propagation of derivatives through all relevant functions. Fig. 2 presents timing benchmarks for a few representative systems: the α -Fe₂O₃(1 $\bar{1}$ 02)-(1 \times 1) surface [14] further discussed in Section VIA, and the Ir(100)-(2 \times 1)O [89], Pt₂₅Rh₇₅(100)-(3 \times 1)O [90], and Pt(111)-(10 \times 10)Te [38] surfaces from Section S14 of the Supporting Information [46]. The mean evaluation times for the R factor (solid symbols) and its gradient (open symbols) are plotted as a function of the cutoff of the angular-momentum quantum number ℓ_{max} . Calculating the gradient increases the computing time by more than an order of magnitude. On the other hand, the information content of the gradient is much larger than that of a single number (n values for n irreducible parameters), and numeric differentiation by finite differences ($n + 1$ evaluations of the R factor) would be slower than automatic differentiation for the larger systems. Consequently, the choice to use gradients involves a tradeoff between higher computational cost and improved efficiency of each optimization step. As discussed in Section V, selective use of gradients is recommended.

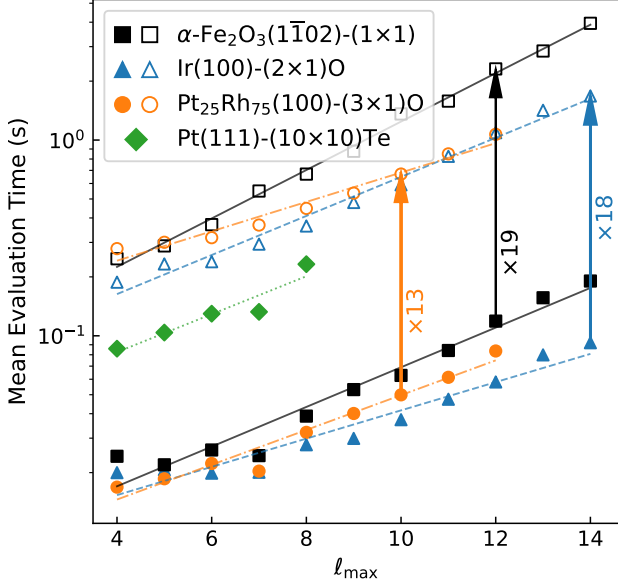


FIG. 2. Timing benchmarks for the calculation of Pendry’s R factor and its gradient for the test systems: $\alpha\text{-Fe}_2\text{O}_3(1\bar{1}02)-(1 \times 1)$ (described in Section VI), $\text{Ir}(100)-(2 \times 1)\text{O}$, and $\text{Pt}_{25}\text{Rh}_{75}(100)-(3 \times 1)\text{O}$ (described in Section S14 of the Supporting Information [46]). The number of free (irreducible) parameters for these systems are 33, 14 and 40 respectively. Timing benchmarks for the evaluation of Pendry’s R factor are also shown for $\text{Pt}(111)-(10 \times 10)\text{Te}$ (119 free parameters; no gradients calculated due to memory limitations, see Section S14 of the Supporting Information [46] for details). The computing times (with an Nvidia A100 GPU) are shown as a function of the angular momentum quantum number cutoff ℓ_{\max} . R -factor evaluations are shown with solid symbols, while gradient evaluations are shown with open symbols. The evaluation time scales almost exponentially with ℓ_{\max} . Dashed lines indicate the exponential fit of the timing data against the cutoff ℓ_{\max} . Arrows indicate the factor by which the gradient calculation is slower than the R -factor calculation at the respective ℓ_{\max} value.

D. Local Refinement

Once a basin in the R -factor hypersurface has been identified by the exploratory search, an algorithm for local optimization can be applied to refine the structure. For this purpose, several algorithms from SciPy’s `optimize.minimize` module [75] were tested, including both gradient-based and gradient-free methods.

The choice of algorithm has a substantial impact on both success rate and runtime. Algorithms suitable for medium- to high-dimensional optimization problems and robust against the small-scale noise [33, 41] in Pendry’s R factor (i.e., the objective function) are particularly advantageous.

An overview of runtimes and R -factor ranges for the

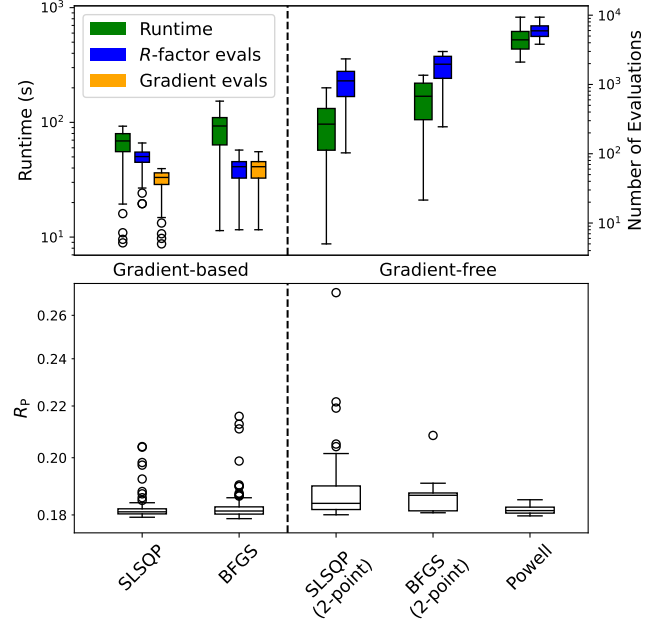


FIG. 3. Comparison of runtime and number of evaluations (top), as well as reliability (bottom) of local optimization algorithms near the global minimum. Algorithms were compared using the second segment (48 irreducible parameters) of the $\alpha\text{-Fe}_2\text{O}_3(1\bar{1}02)-(1 \times 1)$ optimization described in Section VIA, starting from 98 configurations (one per generation) selected from the CMA-ES run. The algorithms shown were found to be the most reliable: sequential least-squares quadratic programming (SLSQP) [91], Broyden–Fletcher–Goldfarb–Shanno (BFGS) [60], and Powell [92, 93], as implemented in SciPy [75]. Gradient-based algorithms are shown to the left of the dashed line, while finite-difference methods are shown to the right. Algorithms labeled as “2-point” employ two-point finite-difference approximations for the gradients. Computational details are provided in Section S3 of the Supporting Information [46]. In each box plot, boxes extend from the first to the third quartile; whiskers extend to the furthest data point within $1.5\times$ of the inter-quartile range. Small circles indicate single outliers beyond the range of the whiskers. Tests using an improved R factor [33] show that outliers in the bottom panel are due to the noisiness of Pendry’s R factor.

most suitable algorithms is presented in Fig. 3. Gradient-based algorithms (left) were more reliable—at comparable runtimes—than their finite-difference counterparts (right). Among these, the sequential least-squares quadratic programming (SLSQP) algorithm [91] and the quasi-Newton Broyden–Fletcher–Goldfarb–Shanno (BFGS) algorithm [60] were found to perform best. While BFGS outperformed SLSQP in certain cases, SLSQP is usually preferable, due to its less frequent use of computationally expensive gradient evaluations, as shown in Fig. 3 (orange).

When gradients are unavailable—for example, due to memory limitations—finite-difference versions of the algorithms provide a reasonable runtime–performance

tradeoff. Powell’s algorithm [92, 93] offers a particularly reliable alternative (as indicated by the lack of outliers in the lower part of Fig. 3), albeit at the cost of a substantially increased runtime (cf. top panel of Fig. 3).

Additional algorithms implemented in SciPy, including COBYLA [94–96], TNC [60, 97], conjugate gradient [60], and Nelder–Mead [98], were also tested but found to be substantially inferior in terms of runtime, reliability, or both. The lower-memory variant L-BFGS-B [99, 100], often recommended for high-dimensional problems, did not outperform SLSQP or BFGS in these tests.

VI. PERFORMANCE BENCHMARKS

To demonstrate the feasibility, and evaluate the performance of the presented tensor-LEED implementation, a series of benchmark tests on several known surface structures were performed. Section VI A shows the results of a structural optimization of $\alpha\text{-Fe}_2\text{O}_3(1\bar{1}02)-(1 \times 1)$, which was used as a main example in the VIPERLEED.CALC publication [14]. Structure optimizations were also performed for the Ir(100)-(2 \times 1)O [89], Pt₂₅Rh₇₅(100)-(3 \times 1)O [90], and Pt(111)-(10 \times 10)Te structures [38], which are discussed in Section S14 of the Supporting Information [46]. [101]

A. $\alpha\text{-Fe}_2\text{O}_3(1\bar{1}02)-(1 \times 1)$

Structural optimization of a bulk-truncated $\alpha\text{-Fe}_2\text{O}_3(1\bar{1}02)-(1 \times 1)$ surface was performed using previously determined values for the incidence angles and the imaginary part of the inner potential [14]. Optimization employed both VIPERLEED-JAX and the TENSERLEED backend in VIPERLEED.CALC. A reference calculation of the initial bulk-truncated structure gives $R_P = 0.747$.

Geometric parameters and vibration amplitudes were optimized in three segments of alternating reference calculations and tensor-LEED-based optimizations. Between these segments, intermediate reference calculations were used to reduce the errors introduced by the tensor-LEED approximation. The parameter ranges were kept consistent between implementations. In the first segment, all atoms in the top two layers were allowed to move in all symmetry-allowed directions, and the vibration amplitudes of the topmost Fe and O atoms were optimized. This corresponds to 30 geometric and 2 vibrational parameters, plus the shift of the real part of the inner potential, for a total of 33 irreducible parameters. In the second and third segments, also the atoms in the third layer were allowed to relax in all symmetry-allowed directions, adding 15 geometric parameters for a total of 48 irreducible parameters.

Both implementations achieve similar Pendry R -factor values after the third segment: $R_P = 0.163$ (TENSERLEED) and $R_P = 0.165$ (VIPERLEED-JAX).

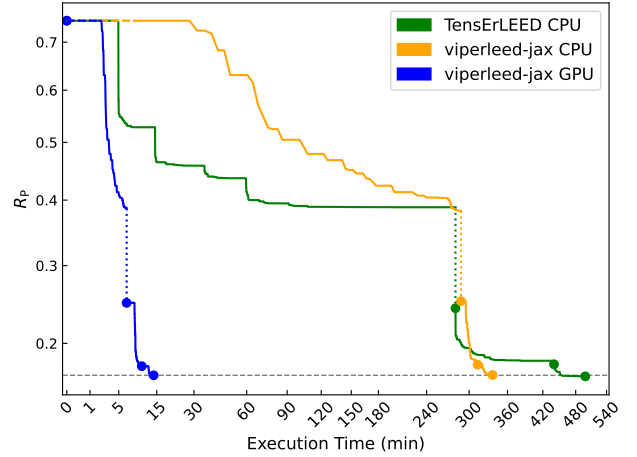


FIG. 4. Comparison of structure optimization for the $\alpha\text{-Fe}_2\text{O}_3(1\bar{1}02)-(1 \times 1)$ surface using VIPERLEED-JAX and the TENSERLEED backend in VIPERLEED.CALC. The running minimum of the R factor is shown as a function of execution time. Optimization proceeds in three segments of alternating reference calculations and tensor-LEED-based optimizations. The starting configuration for each segment corresponds to the final structure of the previous segment, with the first segment beginning from a bulk-truncated structure. R -factor values of the reference calculations are shown as filled circles. Broken horizontal lines indicate the time required for setup and just-in-time compilation in the new tensor-LEED implementation. Dotted vertical lines mark differences in the R factor values between the end of an optimization segment and the subsequent reference calculation, reflecting errors from the perturbative tensor-LEED approximation that are corrected by the reference calculations. A dashed gray line indicates the smallest R -factor value ($R_P = 0.165$) achieved by the new tensor-LEED implementation.

Further refinement is possible with both implementations, but does not aid the discussion here. All differences in geometric and vibration amplitudes are well within the associated fit uncertainties, indicating that both implementations converge towards the same minimum configuration. Minor differences in the final R factor can be attributed to two main sources: Firstly, VIPERLEED-JAX prioritizes numerical accuracy over exact reproduction of the TENSERLEED results. Different implementations of the underlying routines (e.g., interpolation of diffraction intensities) can affect the exact R -factor value. Secondly, as mentioned in Section V D, Pendry’s R factor forms a rough hypersurface with many local minima in the basin [33]. This means that even when using suitable optimization algorithms, it is impossible to gauge whether the optimization result corresponds to the global minimum. This problem disappears when using an improved R factor [33].

The optimization progress is shown in Fig. 4 as R factor versus execution time. Times for the reference calculations (170 s in each segment) are excluded, as they are independent of the tensor-LEED implementa-

tion. To allow for an unbiased comparison, the computing times in Fig. 4 include setup and just-in-time compilation for VIPERLEED-JAX, and the $\delta A_{i,g}$ calculation for the TENSERLEED backend.

On a computing node with 128 CPU cores (AMD 7713) of a modern cluster, VIPERLEED.CALC with the TENSERLEED backend requires approximately 8.5 h for all three segments (green in Fig. 4). With the same hardware, VIPERLEED-JAX completes in less than 5.5 h (orange in Fig. 4). While JAX is not primarily optimized for CPU execution, it still uses just-in-time compilation and thread-based parallelization on CPUs. Running the same calculation on a single Nvidia A100 GPU reduces the total runtime to less than 15 min (blue in Fig. 4).

B. Discussion of the Optimization Process

Using the $\alpha\text{-Fe}_2\text{O}_3(1\bar{1}02)-(1 \times 1)$ example, it is worth taking a closer look at the optimization process. The first optimization segment involves 33 irreducible parameters, automatically identified and analyzed by the parameter-tree algorithm based on the user input.

The first segment employs the two-stage optimization approach described in Section V. In the exploratory stage, CMA-ES searches for the basin containing the global minimum of the R -factor hypersurface. Using generations of 30 individuals, CMA-ES initially explores the parameter space in the wide range given by the parameter bounds, homing in on the region of the global minimum within fewer than 100 generations, corresponding to a runtime of less than 7 min (including setup and just-in-time compilation) on a single Nvidia A100 GPU. This process is illustrated in Fig. 5, where Fig. 5(a) shows the R factor as a function of optimization time, and Fig. 5(b) projects the CMA-ES trajectory onto a two-dimensional subspace of the parameter space obtained by principal-component analysis (PCA). When viewing this plot type, the reader should be aware that the contour lines show the R factor in a plane though the minimum, but there are 31 dimensions orthogonal to the plane plotted. The plane plotted is that with the largest influence on the R factor. In other words, the points sampled (with the exception of the final one) are not exactly in the plane with the contour lines. Thus, the R -factor values along the trajectory in Fig. 5(a) differ from the values in the contour plot. The R factor continuously decreases along the black line in Fig. 5(a) and (b), but this is not seen in the 2D plot of Fig. 5(b), since the 2D projection cannot show all the out-of-plane dimensions. Nevertheless, the plot illustrates that the mean of the CMA-ES population (orange line) approaches the region of the global minimum (yellow).

After the region around the global minimum is located, the optimization switches to the local stage, using the SLSQP algorithm [91] to refine the structure. This decreases the R factor from $R_P = 0.403$ to 0.387 by the end of the first segment. This corresponds to the min-

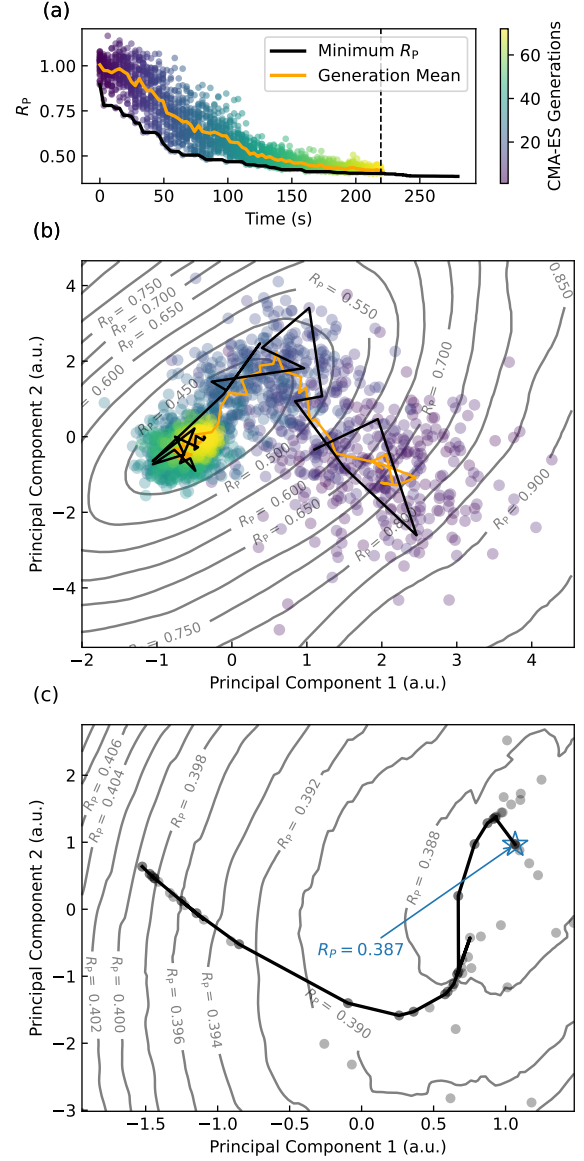


FIG. 5. Structure optimization for $\alpha\text{-Fe}_2\text{O}_3(1\bar{1}02)-(1 \times 1)$ using a two-stage minimization approach. Exploratory and local stages used CMA-ES [86] and SLSQP [75] algorithms, respectively. (a) R_P factor as a function of time. The dashed line marks the switch from the exploratory to the local optimization stage. (b) Points evaluated by the CMA-ES algorithm, projected onto two dimensions using PCA. Colors indicate generation numbers with the same scheme as panel (a). Contour lines display the R -factor in a plane spanned by the first two principal components. The mean and the individual with the smallest R factor for each generation are highlighted by orange and a black lines, respectively. (c) Trajectory of the local optimization, projected onto a 2D plane [different from that of panel (b)] to highlight convergence towards the minimum. Evaluated configurations and the running minimum are represented as individual points and as a black line, respectively. The blue star marks the final configuration with $R_P = 0.387$.

imum of the R -factor hypersurface as calculated in the tensor-LEED approximation based on a perturbation of the initial bulk-truncated surface. The computing time for the local-minimum search is 60 s.

Fig. 5(c) illustrates this stage, where the trajectory is again projected onto a two-dimensional PCA subspace [different from that in Fig. 5(b); again the remaining 31 dimensions cannot be shown]. The contour lines also show the roughness (noisiness) of Pendry’s R factor, which may lead to a partially erratic trajectory; a problem that can be avoided by an improved R factor [33].

The second and third segments proceed similarly but omit the exploratory optimization stage, relying solely on gradient-based refinement. Detailed convergence information for these segments is provided in Section S13 of the Supporting Information [46].

It is worth pointing out that the performance improvements compared with the TENSERLEED search is due to a huge reduction of the number of R -factor evaluations—each including calculation of $I(V)$ curves—rather than just a reduction in the number of $\delta A_{\mathbf{g}}$ calculations. VIPERLEED-JAX and TENSERLEED require a comparable number of $\delta A_{\mathbf{g}}$ evaluations, but the on-the-fly calculation in VIPERLEED-JAX results in a higher overall efficiency [102].

VII. CONCLUSIONS

This work introduces a generalized approach to structure optimization in LEED $I(V)$, extending the VIPERLEED.CALC package. A tree-like representation of the parameter space reduces the problem to an irreducible set of normalized variables, decoupling the optimization from the details of the tensor-LEED technique. This enables the direct use of established bounded optimization algorithms and, compared with earlier LEED- $I(V)$ implementations, leverages decades of development in numerical methods, yielding more robust and efficient refinements.

Central to this work is a fully JAX-based tensor-LEED implementation. Developed entirely in PYTHON, it provides differentiable R -factor calculations and enables gradient-based optimization, marking the first use of non-finite-difference gradients in LEED- $I(V)$ structure determination via tensor LEED.

A two-stage optimization strategy proved particularly effective: CMA-ES for exploration, followed by gradient-based local refinement. This combination consistently identifies the global minimum of the R -factor hypersurface and outperforms the TENSERLEED-based search in VIPERLEED.CALC. As the R -factor evaluation now is a black-box objective function, the new tensor-LEED implementation developed in this work provides the ground for future tests of promising optimization algorithms beyond those examined here, such as particle-swarm optimization [103] and machine-learning-inspired methods

such as Bayesian optimization or stochastic gradient descent [62] on subsets of beams.

For comparability with previous work, the test cases presented here use Pendry’s R factor, which is a noisy objective function for minimization (a “rough” R -factor surface). In terms of both performance and reliability, the gradient-based local refinement will greatly benefit from an improved R factor already implemented in VIPERLEED-JAX, eliminating the roughness and multitude of local R -factor minima in the basin of the global minimum [33].

Although developed for tensor LEED, the principles are general and may also be valuable for other methods like surface x-ray diffraction. The modular code design supports future extensions, such as additional constraints or nonstructural parameters.

VIII. DATA AND CODE AVAILABILITY

The source code for VIPERLEED-JAX is available online in Ref. 72 under the GNU General Public License version 3 (or later) [73]. The raw data used for the examples presented in this work are available at [101].

IX. AUTHOR CONTRIBUTIONS

A.M.I. conceived the presented formalism. A.M.I. and P.H. developed the tensor-LEED software implementation and structure-optimization routines. The technical implementation was aided by F.K., R.W., F.B., T.H., and M.R.. S.T., M.K., J.C., G.K.H.M., M.S., and U.D. supported development of the main ideas and data analysis. M.S., U.D., and M.R. supervised the project. The manuscript was drafted by A.M.I. with input from all authors.

X. COMPETING INTERESTS

The authors declare no competing interests.

ACKNOWLEDGMENTS

The authors would like to thank Lutz Hammer for carefully reading the manuscript and many helpful suggestions. This research was funded in part by the Austrian Science Fund (FWF) under doi:10.55776/F8100, Taming Complexity in Materials Modeling (TACO), and under doi:10.55776/J4811 (F.K.), as well as by the European Research Council (ERC) under the European Union’s Horizon 2020 research and innovation programme (grant agreement No. 883395, Advanced Research Grant ‘Wat-Fun’). J.C. acknowledges grant CEX2023-001286-S funded by MICIU/AEI doi:10.13039/501100011033 and grant PID2023-148359NB-C21 funded by MICIU/AEI

doi:10.13039/501100011033 and the European Union FEDER. The computational results presented have been achieved in part using the Austrian Scientific Computing (ASC) infrastructure. For the purpose of open access,

the authors have applied a CC BY public copyright license to any Author Accepted Manuscript version arising from this submission.

-
- [1] J. B. Pendry, *Low Energy Electron Diffraction: The Theory and Its Application to Determination of Surface Structure*, Techniques of Physics No. 2 (Academic Press, London, 1974).
- [2] M. A. Van Hove and S. Y. Tong, *Surface Crystallography by LEED*, edited by V. I. Goldanskii, R. Gomer, F. P. Schäfer, and J. P. Toennies, Springer Series in Chemical Physics, Vol. 2 (Springer, Berlin, Heidelberg, 1979).
- [3] M. A. Van Hove, W. H. Weinberg, and C.-M. Chan, *Low-Energy Electron Diffraction: Experiment, Theory and Surface Structure Determination*, edited by G. Ertl and R. Gomer, Springer Series in Surface Sciences, Vol. 6 (Springer, Berlin, Heidelberg, 1986).
- [4] W. Moritz and M. A. Van Hove, *Surface Structure Determination by LEED and X-rays*, 1st ed. (Cambridge University Press, 2022).
- [5] K. Heinz, Electron based methods: 3.2.1 Low-energy electron diffraction (LEED), in *Surface and Interface Science*, edited by K. Wandelt (John Wiley & Sons, Ltd., 2013) Chap. 3.2, pp. 93–150.
- [6] D. Woodruff, 60 years of surface structure determination, *Surf. Sci.* **749**, 122552 (2024).
- [7] G. Held, Structure determination by low-energy electron diffraction—A roadmap to the future, *Surf. Sci.* **754**, 122696 (2025).
- [8] T. Fauster, L. Hammer, K. Heinz, and M. A. Schneider, *Surface Physics: Fundamentals and Methods* (De Gruyter Oldenbourg, 2020).
- [9] M. P. Seah and W. A. Dench, Quantitative electron spectroscopy of surfaces: A standard data base for electron inelastic mean free paths in solids, *Surf. Interface Anal.* **1**, 2 (1979).
- [10] D. K. Saldin and X. Chen, Three-dimensional reconstruction by holographic LEED: Proper identification of the reference wave, *Phys. Rev. B* **52**, 2941 (1995).
- [11] K. Reuter, J. Scharadt, J. Bernhardt, H. Wedler, U. Starke, and K. Heinz, LEED holography applied to a complex superstructure: A direct view of the adatom cluster on SiC(111)-(3 × 3), *Phys. Rev. B* **58**, 10806 (1998).
- [12] D. K. Saldin, A. Seubert, and K. Heinz, Solution of a multiple-scattering inverse problem: Electron diffraction from surfaces, *Phys. Rev. Lett.* **88**, 115507 (2002).
- [13] C. Y. Chang, Z. C. Lin, Y. C. Chou, and C. M. Wei, Direct three-dimensional Patterson inversion of low-energy electron diffraction $i(e)$ curves, *Phys. Rev. Lett.* **83**, 2580 (1999).
- [14] F. Kraushofer, A. M. Imre, G. Franceschi, T. Kißlinger, E. Rheinfrank, M. Schmid, U. Diebold, L. Hammer, and M. Riva, ViPerLEED package I: Calculation of $I(V)$ curves and structural optimization, *Phys. Rev. Res.* **7**, 013005 (2025).
- [15] S. Y. Tong, Theory of low-energy electron diffraction, *Prog. Surf. Sci.* **7**, 1 (1975).
- [16] M. A. Van Hove, W. Moritz, H. Over, P. J. Rous, A. Wander, A. Barbieri, N. Materer, U. Starke, and G. A. Somorjai, Automated determination of complex surface structures by LEED, *Surf. Sci. Rep.* **19**, 191 (1993).
- [17] M. Blanco-Rey, P. De Andres, G. Held, and D. A. King, A FORTRAN-90 low-energy electron diffraction program (LEED90 v1.1), *Comput. Phys. Commun.* **161**, 151 (2004).
- [18] A. Wander, A new modular low energy electron diffraction package — DLLEED, *Comput. Phys. Commun.* **137**, 4 (2001).
- [19] D. J. Titterton and C. G. Kinniburgh, Calculation of LEED diffracted intensities, *Comput. Phys. Commun.* **20**, 237 (1980).
- [20] G. Held, M. P. Bessent, S. Titmuss, and D. A. King, Realistic molecular distortions and strong substrate buckling induced by the chemisorption of benzene on Ni{111}, *J. Chem. Phys.* **105**, 11305 (1996).
- [21] V. Blum and K. Heinz, Fast LEED intensity calculations for surface crystallography using tensor LEED, *Comput. Phys. Commun.* **134**, 392 (2001).
- [22] J. Lachnitt, AQUALEED, <https://jan.lachnitt.cz/aqualeed.en.html>.
- [23] <https://github.com/empa-scientific-it/cleedpy>.
- [24] J. Rundgren, Optimized surface-slab excited-state muffin-tin potential and surface core level shifts, *Phys. Rev. B* **68**, 125405 (2003).
- [25] J. Rundgren, Elastic electron-atom scattering in amplitude-phase representation with application to electron diffraction and spectroscopy, *Phys. Rev. B* **76**, 195441 (2007).
- [26] J. Rundgren, B. E. Sernelius, and W. Moritz, Low-energy electron diffraction with signal electron carrier-wave wavenumber modulated by signal exchange-correlation interaction, *J. Phys. Commun.* **5**, 105012 (2021).
- [27] N. Materer, U. Starke, A. Barbieri, R. Döll, K. Heinz, M. A. Van Hove, and G. A. Somorjai, Reliability of detailed LEED structural analyses: Pt(111) and Pt(111)-p(2×2)-O, *Surf. Sci.* **325**, 207 (1995).
- [28] P. J. Feibelman, DFT versus the “real world” (or, waiting for Godft), *Top. Catal.* **53**, 417 (2010).
- [29] E. Zanazzi and F. Jona, A reliability factor for surface structure determinations by low-energy electron diffraction, *Surf. Sci.* **62**, 61 (1977).
- [30] J. B. Pendry, Reliability factors for LEED calculations, *J. Phys. C: Solid State Phys.* **13**, 937 (1980).
- [31] S. P. Tear, K. Roll, and M. Prutton, A comparison of reliability (R) factors in a LEED structural analysis of the copper (111) surface, *J. Phys. C: Solid State Phys.* **14**, 3297 (1981).
- [32] M. Sporn, E. Platzgummer, S. Forsthuber, M. Schmid, W. Hofer, and P. Varga, The accuracy of quantitative LEED in determining chemical composition profiles of

- substitutionally disordered alloys: A case study, *Surf. Sci.* **416**, 423 (1998).
- [33] A. M. Imre, L. Hammer, U. Diebold, M. Riva, and M. Schmid, *An improved reliability factor for quantitative low-energy electron diffraction* (2025), [arXiv:2511.05448 \[cond-mat.mtrl-sci\]](https://arxiv.org/abs/2511.05448).
- [34] F. Jona, K. O. Legg, H. D. Shih, D. W. Jepsen, and P. M. Marcus, Random occupation of adsorption sites in the $c(2 \times 2)$ structure of CO on Fe{001}, *Phys. Rev. Lett.* **40**, 1466 (1978).
- [35] Further non-structural parameters are the angle of incidence of the electron beam or the imaginary part of the inner potential, V_{0i} , which describes the attenuation by inelastic scattering. These parameters cannot be optimized with today's tensor-LEED method (see [Section IC](#)) and are therefore not considered here. The methods for optimizing these parameters in ViPerLEED [14] are not modified by the current work.
- [36] The computationally most expensive part of a full-dynamic calculation for large unit cells is the inversion of several $d \times d$ matrices, $d = N(\ell_{\max} + 1)^2$ with N being the number of scattering centers in the unit cell per layer and ℓ_{\max} being the maximum angular-momentum quantum number used in the calculation [1, 15]. Depending on the case and algorithm used, the computational effort for matrix inversions scales like $d^{2.38}$ to d^3 [14].
- [37] W. Moritz, B. Wang, M.-L. Bocquet, T. Brugger, T. Greber, J. Wintterlin, and S. Günther, Structure Determination of the Coincidence Phase of Graphene on Ru(0001), *Phys. Rev. Lett.* **104**, 136102 (2010).
- [38] T. Kißlinger, A. Schewski, A. Raabgrund, H. Loh, L. Hammer, and M. A. Schneider, Surface telluride phases on Pt(111): Reconstructive formation of unusual adsorption sites and well-ordered domain walls, *Phys. Rev. B* **108**, 205412 (2023).
- [39] P. J. Rous, J. B. Pendry, D. K. Saldin, K. Heinz, K. Müller, and N. Bickel, Tensor LEED: A technique for high-speed surface-structure determination, *Phys. Rev. Lett.* **57**, 2951 (1986).
- [40] P. J. Rous and J. B. Pendry, The theory of tensor LEED, *Surf. Sci.* **219**, 355 (1989).
- [41] P. J. Rous, The tensor-LEED approximation and surface crystallography by low-energy electron diffraction, *Prog. Surf. Sci.* **39**, 3 (1992).
- [42] U. Löffler, R. Döll, K. Heinz, and J. B. Pendry, Investigation of surface atom vibrations by tensor LEED, *Surf. Sci.* **301**, 346 (1994).
- [43] R. Döll, M. Kottcke, and K. Heinz, Chemical substitution of surface atoms in structure determination by tensor low-energy electron diffraction, *Phys. Rev. B* **48**, 1973 (1993).
- [44] K. Heinz, R. Döll, and M. Kottcke, Tensor LEED for the geometrical and chemical structure of alloy surfaces, *Surf. Rev. Lett.* **3**, 1651 (1996).
- [45] The original formulation allows different levels of sophistication for modeling the effects of geometric displacements, with correspondingly different computational cost. Rous *et al.* [39] suggested a middle-ground approach in which individual atomic displacements affect the atomic t matrices, while mixed terms involving multiple atoms are neglected.
- [46] See Supporting Information at [URL](#) for more details concerning: (S1) Non-linearity of amplitude changes; (S2) interaction of ViPerLEED-JAX with external optimizers; (S3) computational details; (S4) notes on the technical implementation; (S5) tree-based dependent quantities; (S6) nonstructural parameters and interpolation; (S7) interpretation of user-supplied constraints and bounds; (S8) notes on parameter types; (S9) treatment of parameter bounds; (S10) post-processing of occupancy parameters; (S11) implementation of bounds in CMA-ES; (S12) preconditioning of gradient-based optimization; (S13) continued optimization of the α -Fe₂O₃(1102)-(1 × 1) example; (S14) further examples and practical considerations.
- [47] M. Schmid, F. Kraushofer, A. M. Imre, T. Kißlinger, L. Hammer, U. Diebold, and M. Riva, ViPerLEED package II: Spot tracking, extraction, and processing of $I(V)$ curves, *Phys. Rev. Res.* **7**, 013006 (2025).
- [48] F. Dörr, M. Schmid, L. Hammer, U. Diebold, and M. Riva, ViPerLEED package III: Data acquisition for quantitative low-energy electron diffraction, in preparation (2025).
- [49] ViPerLEED documentation, <https://www.viperleed.org>.
- [50] The ViPerLEED source code is available on GitHub under <https://github.com/viperleed/viperleed>. TENSORLEED 2.0 is available under <https://github.com/viperleed/viperleed-tensorleed>. For more information on the usage and installation, see <https://www.viperleed.org> [49].
- [51] M. Kottcke and K. Heinz, A new approach to automated structure optimization in LEED intensity analysis, *Surf. Sci.* **376**, 352 (1997).
- [52] P. G. Cowell and V. E. De Carvalho, Unconstrained optimisation in surface crystallography by LEED: Preliminary results of its application to CdTe(110), *Surf. Sci.* **187**, 175 (1987).
- [53] G. Kleinle, W. Moritz, D. L. Adams, and G. Ertl, A novel procedure for fast surface structural analysis based on LEED intensity data, *Surf. Sci. Lett.* **219**, L637 (1989).
- [54] G. Kleinle, W. Moritz, and G. Ertl, An efficient method for LEED crystallography, *Surf. Sci.* **238**, 119 (1990).
- [55] P. J. Rous, M. A. Van Hove, and G. A. Somorjai, Directed search methods for surface structure determination by LEED, *Surf. Sci.* **226**, 15 (1990).
- [56] H. Over, U. Ketterl, W. Moritz, and G. Ertl, Optimization methods and their use in low-energy electron-diffraction calculations, *Phys. Rev. B* **46**, 15438 (1992).
- [57] P. J. Rous, A global approach to the search problem in surface crystallography by low-energy electron diffraction, *Surf. Sci.* **296**, 358 (1993).
- [58] R. Döll and M. A. Van Hove, Global optimization in LEED structure determination using genetic algorithms, *Surf. Sci.* **355**, L393 (1996).
- [59] V. B. Nascimento and E. W. Plummer, Differential evolution: Global search problem in LEED-IV surface structural analysis, *Mater. Charact.* **100**, 143 (2015).
- [60] J. Nocedal and S. Wright, *Numerical Optimization* (Springer Science & Business Media, 2006).
- [61] J. F. Bonnass, J. C. Gilbert, C. Lemaréchal, and C. A. Sagastizábal, *Numerical Optimization* (Springer, Berlin, Heidelberg, 2006).
- [62] M. J. Kochenderfer and T. A. Wheeler, *Algorithms for Optimization* (The MIT press, Cambridge, 2019).
- [63] C. C. Margossian, A review of automatic differentiation and its efficient implementation, *WIREs Data Min.*

Knowl. Discov. **9**, e1305 (2019).

- [64] A. G. Baydin, B. A. Pearlmutter, A. A. Radul, and J. M. Siskind, Automatic differentiation in machine learning: A survey, *J. Mach. Learn. Res.* **18**, 5595 (2017).
- [65] A. Griewank, Who invented the reverse mode of differentiation?, in *Optimization Stories*, Documenta Mathematica Series, Vol. 6, edited by M. Grötschel (EMS Press, 2012) pp. 389–400.
- [66] M. Abadi, A. Agarwal, P. Barham, E. Brevdo, Z. Chen, C. Citro, G. S. Corrado, A. Davis, J. Dean, M. Devin, S. Ghemawat, I. Goodfellow, A. Harp, G. Irving, M. Isard, Y. Jia, R. Jozefowicz, L. Kaiser, M. Kudlur, J. Levenberg, D. Mané, R. Monga, S. Moore, D. Murray, C. Olah, M. Schuster, J. Shlens, B. Steiner, I. Sutskever, K. Talwar, P. Tucker, V. Vanhoucke, V. Vasudevan, F. Viégas, O. Vinyals, P. Warden, M. Wattenberg, M. Wicke, Y. Yu, and X. Zheng, *TensorFlow: Large-scale machine learning on heterogeneous systems* (2015), doi:10.5281/zenodo.4724125.
- [67] J. Ansel, E. Yang, H. He, N. Gimelshein, A. Jain, M. Voznesensky, B. Bao, P. Bell, D. Berard, E. Burovski, G. Chauhan, A. Chourdia, W. Constable, A. Desmaison, Z. DeVito, E. Ellison, W. Feng, J. Gong, M. Gschwind, B. Hirsh, S. Huang, K. Kalambarkar, L. Kirsch, M. Lazos, M. Lezcano, Y. Liang, J. Liang, Y. Lu, C. K. Luk, B. Maher, Y. Pan, C. Puhersch, M. Reso, M. Saroufim, M. Y. Siraichi, H. Suk, S. Zhang, M. Suo, P. Tillet, X. Zhao, E. Wang, K. Zhou, R. Zou, X. Wang, A. Mathews, W. Wen, G. Chanan, P. Wu, and S. Chintala, PyTorch 2: Faster machine learning through dynamic Python bytecode transformation and graph compilation, in *Proceedings of the 29th ACM International Conference on Architectural Support for Programming Languages and Operating Systems, Volume 2*, ASPLOS '24 (Association for Computing Machinery, New York, NY, USA, 2024) pp. 929–947.
- [68] J. Bradbury, R. Frostig, P. Hawkins, M. J. Johnson, C. Leary, D. Maclaurin, G. Necula, A. Paszke, J. VanderPlas, S. Wanderman-Milne, and Q. Zhang, *JAX: Composable transformations of Python+NumPy programs* (2018), <http://github.com/google/jax>.
- [69] The occupancy parameters c_i require a non-linear post-processing step. In the parameter-tree formalism, dummy occupancy parameters are used, which are converted to physical occupancies at a later stage. This transformation is detailed in Sections S2, S8 and S10 of the Supporting Information [46].
- [70] For an injective linear transformation with associated matrix A , a left pseudoinverse A^+ exists such that
- $$A^+A = \mathbb{I}, \quad (19)$$
- where \mathbb{I} is the identity matrix. The pseudoinverse is
- $$A^+ = (A^*A)^{-1}A^*, \quad (20)$$
- with A^* the Hermitian conjugate of A . For real-valued transformation matrices, A^* is replaced by the transpose A^T . Thus, the inverse of an injective linear transformation $X_{n,m}$ in the parameter tree is
- $$X_{m,n} = M_{n,m}^+ = (M_{n,m}^T M_{n,m})^{-1} M_{n,m}^T, \quad (21)$$
- where $M_{n,m}$ is the (real-valued) matrix representation of the linear transformation $X_{n,m}$.
- [71] G. M. Ziegler, *Lectures on Polytopes*, Graduate Texts in Mathematics, Vol. 152 (Springer, New York, NY, 1995).
- [72] <https://github.com/viperleed/viperleed-jax>.
- [73] <https://www.gnu.org/licenses/gpl-3.0.en.html>.
- [74] C. R. Harris, K. J. Millman, S. J. van der Walt, R. Gommers, P. Virtanen, D. Cournapeau, E. Wieser, J. Taylor, S. Berg, N. J. Smith, R. Kern, M. Picus, S. Hoyer, M. H. van Kerkwijk, M. Brett, A. Haldane, J. F. del Río, M. Wiebe, P. Peterson, P. Gérard-Marchant, K. Sheppard, T. Reddy, W. Weckesser, H. Abbasi, C. Gohlke, and T. E. Oliphant, Array programming with NumPy, *Nature* **585**, 357 (2020).
- [75] P. Virtanen, R. Gommers, T. E. Oliphant, M. Haberland, T. Reddy, D. Cournapeau, E. Burovski, P. Peterson, W. Weckesser, J. Bright, S. J. van der Walt, M. Brett, J. Wilson, K. J. Millman, N. Mayorov, A. R. J. Nelson, E. Jones, R. Kern, E. Larson, C. J. Carey, Í. Polat, Y. Feng, E. W. Moore, J. VanderPlas, D. Laxalde, J. Perktold, R. Cimrman, I. Henriksen, E. A. Quintero, C. R. Harris, A. M. Archibald, A. H. Ribeiro, F. Pedregosa, P. van Mulbregt, and SciPy 1.0 Contributors, SciPy 1.0: Fundamental algorithms for scientific computing in Python, *Nat. Methods* **17**, 261 (2020).
- [76] <https://github.com/c0fec0de/anytree>.
- [77] H. Montes-Campos, J. Carrete, S. Bichelmaier, L. M. Varela, and G. K. H. Madsen, A differentiable neural-network force field for ionic liquids, *J. Chem. Inf. Model.* **62**, 88 (2022).
- [78] R. Conlin, INTERPAX, doi:10.5281/zenodo.10028967.
- [79] A. Meurer, C. P. Smith, M. Paprocki, O. Čertík, S. B. Kirpichev, M. Rocklin, Am. Kumar, S. Ivanov, J. K. Moore, S. Singh, T. Rathnayake, S. Vig, B. E. Granger, R. P. Muller, F. Bonazzi, H. Gupta, S. Vats, F. Johansson, F. Pedregosa, M. J. Curry, A. R. Terrel, Š. Roučka, A. Saboo, I. Fernando, S. Kulal, R. Cimrman, and A. Scopatz, SymPy: Symbolic computing in Python, *PeerJ Comput. Sci.* **3**, e103 (2017).
- [80] J. Rasch and A. C. H. Yu, Efficient storage scheme for precalculated Wigner 3- j , 6- j and Gaunt coefficients, *SIAM J. Sci. Comput.* **25**, 1416 (2004).
- [81] D. H. Wolpert and W. G. Macready, No free lunch theorems for optimization, *IEEE Trans. Evol. Comput.* **1**, 67 (1997).
- [82] F. Schoen, Two-phase methods for global optimization, in *Handbook of Global Optimization*, Vol. 62, edited by P. M. Pardalos, P. M. Pardalos, and H. E. Romeijn (Springer US, Boston, MA, 2002) pp. 151–177.
- [83] D. J. Wales and J. P. K. Doye, Global optimization by basin-hopping and the lowest energy structures of lennard-jones clusters containing up to 110 atoms, *J. Phys. Chem. A* **101**, 5111 (1997).
- [84] N. Hansen and A. Ostermeier, Completely derandomized self-adaptation in evolution strategies, *Evol. Comput.* **9**, 159 (2001).
- [85] N. Hansen, *The CMA evolution strategy: A tutorial* (2023), [arXiv:1604.00772](https://arxiv.org/abs/1604.00772).
- [86] R. Wanzelböck, F. Buchner, P. Kovács, G. K. H. Madsen, and J. Carrete, Clinamen2: Functional-style evolutionary optimization in Python for atomistic structure searches, *Comput. Phys. Commun.* **297**, 109065 (2024).
- [87] O. M. Shir and A. Yehudayoff, On the covariance–Hessian relation in evolution strategies, *Theor. Comput.*

- Sci. **801**, 157 (2020).
- [88] M. Abramowitz and I. A. Stegun, *Handbook of Mathematical Functions with Formulas, Graphs, and Mathematical Tables* (Dover, New York, 1964).
 - [89] P. Ferstl, T. Schmitt, M. A. Schneider, L. Hammer, A. Michl, and S. Müller, Structure and ordering of oxygen on unreconstructed Ir(100), *Phys. Rev. B* **93**, 235406 (2016).
 - [90] M. Sporn, E. Platzgummer, E. L. D. Gruber, M. Schmid, W. Hofer, and P. Varga, A quantitative LEED analysis of the oxygen-induced $p(3\times 1)$ reconstruction of $\text{Pt}_{25}\text{Rh}_{75}(100)$, *Surf. Sci.* **416**, 384 (1998).
 - [91] D. Kraft, *A Software Package for Sequential Quadratic Programming* (Wiss. Berichtswesen d. DFVLR, 1988).
 - [92] M. J. D. Powell, An efficient method for finding the minimum of a function of several variables without calculating derivatives, *Comput. J.* **7**, 155 (1964).
 - [93] W. H. Press, ed., *Numerical Recipes: The Art of Scientific Computing*, 3rd ed. (Cambridge University Press, Cambridge, 2007).
 - [94] M. J. D. Powell, A direct search optimization method that models the objective and constraint functions by linear interpolation, in *Advances in Optimization and Numerical Analysis*, edited by S. Gomez and J.-P. Henrart (Springer Netherlands, Dordrecht, 1994) pp. 51–67.
 - [95] M. J. D. Powell, Direct search algorithms for optimization calculations, *Acta Numer.* **7**, 287 (1998).
 - [96] M. J. D. Powell, A view of algorithms for optimization without derivatives, *Math. Today-Bull. Inst. Math. Appl.* **43**, 170 (2007).
 - [97] S. G. Nash, Newton-type minimization via the Lanczos method, *SIAM J. Numer. Anal.* **21**, 770 (1984).
 - [98] J. A. Nelder and R. Mead, A simplex method for function minimization, *Comput. J.* **7**, 308 (1965).
 - [99] R. H. Byrd, P. Lu, J. Nocedal, and C. Zhu, A limited memory algorithm for bound constrained optimization, *SIAM J. Sci. Comput.* **16**, 1190 (1995).
 - [100] C. Zhu, R. H. Byrd, P. Lu, and J. Nocedal, Algorithm 778: L-BFGS-B: Fortran subroutines for large-scale bound-constrained optimization, *ACM Trans. Math. Softw.* **23**, 550 (1997).
 - [101] Supplementary dataset for structural optimization in tensor LEED using a parameter tree and R-factor gradients, <https://doi.org/10.48436/xsptw-81983>.
 - [102] In VIPERLEED-JAX, approximately 2.3×10^3 R -factor values were evaluated in the first segment of the $\alpha\text{-Fe}_2\text{O}_3(1\bar{1}02)-(1 \times 1)$ example. In contrast, the algorithm of Kottcke and Heinz [51], as used in TENSERLEED, requires about 5.7×10^5 generations with 128 individuals each to reach the same R -factor value, corresponding to roughly 7×10^7 R -factor evaluations. In VIPERLEED-JAX, R -factor evaluations are directly coupled with the $\delta A_{i,\mathbf{g}}$ calculations, resulting in approximately 2.3×10^3 $\delta A_{i,\mathbf{g}}$ evaluations per atom under variation, yielding about 7×10^4 evaluations for the 30 atoms in the first stage. In TENSERLEED, $\delta A_{\mathbf{g}}$ values are only evaluated during the “delta-amplitude calculation”, where they are pre-computed on a user-defined grid. In the first segment of the $\alpha\text{-Fe}_2\text{O}_3(1\bar{1}02)-(1 \times 1)$ example, a grid of 11, 7, and 7 geometric steps in x , y , and z directions, respectively, was used for each of the 30 perturbed atoms. The four topmost atoms were additionally allowed 9 different vibration-amplitude values, which were varied together with the z coordinate. Altogether, this yields $26 \times (11 + 7 + 7) + 4 \times (11 \times 9 + 7 + 7) = 1102$ atomic $\delta A_{i,\mathbf{g}}$ evaluations per search loop, and around 17×10^4 evaluations for the 16 loops required for convergence.
 - [103] D. A. Duncan, J. I. J. Choi, and D. P. Woodruff, Global search algorithms in surface structure determination using photoelectron diffraction, *Surf. Sci.* **606**, 278 (2012).